Available online at www.sciencedirect.com
ScienceDirect
Trans. Nonferrous Met. Soc. China 34(2024) 50−64
Transactions of Nonferrous Metals Society of China
www.tnmsc.cn

Reinforcing effects of nano-WC in AlSi10Mg alloy assisted by in-situ surface modification approach

Jiang-long YI[1], Han-lin LIAO[2,3], Cheng CHANG[2,3], Xing-chen YAN[2], Min LIU[2], Ke-song ZHOU[1,2]

1. College of Materials and Energy, Guangdong University of Technology, Guangzhou 510006, China;
2. Guangdong Provincial Key Laboratory of Modern Surface Engineering Technology, National Engineering Laboratory for Modern Materials Surface Engineering Technology, Institute of New Materials, Guangdong Academy of Sciences, Guangzhou 510651, China;
3. ICB UMR 6303, CNRS, Univ. Bourgogne Franche-Comté, UTBM, 90010, Belfort, France

Received 14 June 2022; accepted 28 September 2022

Abstract: A series of nano-WC surface modified AlSi10Mg powders with different WC contents were synthesized by the electrostatic assembly method. After the selective laser melting (SLM) processing, various Al−W intermetallics were in-situ formed in the SLM nano-WC/AlSi10Mg composites. A well-coherent Al/Al_5W interface with a low lattice mismatch of 4.7% was confirmed with an orientation relationship of $(002)_{\alpha(Al)}//(104)_{Al_5W}$. The nano-WC particles and Al−W intermetallics triggered the columnar-to-equiaxed transition, leading to a fine equiaxed microstructure. As a result, the SLMed 3 wt.% nano-WC/AlSi10Mg composites showed remarkable mechanical properties, with an ultimate tensile strength of (464.1±8.68) MPa and elongation of (5.6±0.95)%. Additionally, the SLMed 3 wt.% WC/AlSi10Mg samples also achieved the lowest average coefficient of friction (0.429) and wear rate of 3.842×10^{-5} $mm^3/(N\cdot m)$ compared to other WC/AlSi10Mg composites. The remarkable mechanical and wear properties are ascribed to fine-grain and second-phase strengthening.

Key words: in-situ modification; selective laser melting; nano-WC; AlSi10Mg; mechanical properties

1 Introduction

With urgent demands for the structural components possessing high-performance materials and sophisticated geometries in various application fields, the fabrication of low-density and high-strength materials using selective laser melting (SLM) technology has become one of the current research hotspots [1−3]. More and more attention has been grasped to the SLM-fabricated aluminum (Al)-based parts owing to the low density (~2.7 g/cm^3), high specific strength (50−130 $MPa/(g\cdot cm^{-3})$), and excellent fracture toughness (20−50 $MPa\cdot m^{-1/2}$) [4,5]. However, the traditional Al-based alloys are normally designed and manufactured based on the casting or forging process characteristics. On the one hand, the inherent nature of Al-based materials, such as low absorption of infrared laser, poor weldability, and sensitivity to thermal cracking, leads to only a few categories of aluminum alloys suitable for SLM manufacturing. On the other hand, some aluminum alloys with favorable weldability (e.g., Al−Si alloys [6]) manufactured using SLM are always composed of coarse columnar grains, resulting in relatively low mechanical properties. Hence, the exploration and development of high-performance Al-based materials adapted for SLM have aroused intensive interest in the SLM.

Corresponding author: Xing-chen YAN, E-mail: yanxingchen@gdinm.com
DOI: 10.1016/S1003-6326(23)66381-2

To ameliorate the mechanical properties of the SLM Al-based materials, micro-/nano-reinforcements are introduced into the aluminum matrix composites (AMCs) feedstocks via mechanical ball milling method. After the milling treatment for the 2 wt.% SiC/AlSi7Mg powders, WANG et al [7] obtained AMCs with excellent mechanical properties (i.e., UTS of (502.94±6.40) MPa, elongation of (10.64±1.06)%). XI et al [8] fabricated a carbon nanotube-enhanced SLM Al−Mg−Sc−Zr alloy using the ball milling method. They found that the in-situ formed Al_4C_3 phase can boost the strength of the SLMed Al−Mg−Sc−Zr alloy from (382.2±8.1) to (409.4±5.4) MPa. Moreover, LI et al [9] prepared micro-TiB_2/AlSi10Mg alloy after experiencing a high-energy ball milling process. They reported that a higher tensile strength of 380 MPa can be attained even with a trace amount of ceramic particles addition. Although many researchers proved that high-property AMCs could be obtained via ball-milling micro-/nano-ceramics with Al-based powders, the powder deformation phenomenon could be easily generated during material syntheses, thus leading to a poor powder spreading process during the SLM. It could be concluded in reported literatures that the addition of ceramic particles would deteriorate the flowability of the matrix powders [10,11]. Meanwhile, the powder particles might fracture, cold weld, and even refracture during the mechanical mixing process, which have an impact on the laser melt behavior of AMCs. Additionally, owing to the van der Waals force, the nano-ceramic particles tend to agglomerate after ball milling [9].

Thus, researchers have been focused on how to prevent nanoparticle aggregation and investigate novel methods to fabricate AMCs, such as electro-static assembly [12], aerosol delivered adhesion [13], ultrasonic vibration dispersion [14], gas-atomization [15], and friction stir processing [16]. MARTIN et al [17] provided a promising manufacturing method to reduce the agglomerative tendency of nanoparticles. The electrostatic assembly technique was used to fabricate a series of aluminum alloy powders decorated with the lattice-matched nanoparticle and the SLM 7075 alloy without hot tearing cracks was successfully synthesized, which exhibited high mechanical performance. LI et al [18] fabricated an in-situ nano-TiB_2 decorated AlSi10Mg composite powder by gas-atomization and investigated the effect of TiB_2 nanoparticles in the SLM AlSi10Mg alloy. Their works reveal that both the nano-TiB_2 and nano-Si precipitates indicated a solid interfacial bonding with the Al matrix. As a result, the SLM nano-TiB_2 reinforced AlSi10Mg exhibited a high microhardness (~191 ($HV_{0.3}$)), tensile strength (~530 MPa) and excellent ductility (~15.5%).

It is well known that nano-WC particles usually have some outstanding benefits in wear resistance and mechanical properties. As reported by LI et al [19], the nano-WC reinforced Co-based laser cladding layer exhibited better metallurgical bonding and finer grains than the micro-WC cladding layer, which improves the wear resistance of the nano-WC cladding layers. Hence, the nano-WC particles were selected as the reinforcing phase added into the AlSi10Mg matrix to fabricate high-performance Al-based nanocomposites by SLM. To cope with the large attractive effect to van der Waals forces between the nano-WC particles, the novel electrostatic self-assembly method was used to prepare the nano-WC/AlSi10Mg powder. Notably, there are still a few studies about the nano-WC reinforced AlSi10Mg alloy even though a modest mismatch (2.2%) existed within the $(111)_{\alpha(Al)}/(001)_{WC}$ interface [20]. Hence, different contents of the nano-WC in-situ surface-modified AlSi10Mg powder were fabricated, and the reinforcing effects were carefully investigated in this research. Meanwhile, the optimization of nano-WC content was determined by characterizing their microstructural evaluation, mechanical properties and wear performance. This research was focused on expanding the application of SLM Al-based nanocomposites based on their remarkable mechanical properties and wear resistance. Meanwhile, the nano-WC particle reinforced aluminum matrix composites showed the potential to meet the combination requirements of mechanical and functional properties in industrial applications.

2 Experimental

2.1 Materials preparation

AlSi10Mg powder with the size of 17−53 μm was purchased from the company of Beijing Baohang Advanced Materials Co. Ltd. (China). Nano-WC powder with an average size of 200 nm

used in this work was produced by Xuzhou Jiechuang New Materials Technology Co., Ltd., (China). To obtain the nano-WC in-situ surface modified AlSi10Mg powder, each gram of AlSi10Mg powder was dispersed in 100 mL of ethanol aqueous solution (1:1) firstly. 1 mL of (3-aminopropyl) triethoxysilane (APTES, 99%, Aladdin) was added to the above solution to attain the amine functionalized AlSi10Mg powder. Afterward, 1 g of WC nanoparticles was dispersed in 1 L of deionized water containing 1 mL of sodium dodecyl sulfate (SDS, 99.0%, Aladdin). The above two solutions were mixed and stirred for 1 h. A series of nano-WC/AlSi10Mg powders with different WC contents (i.e., 1 wt.%, 3 wt.% and 5 wt.%) were fabricated and then filtered in a vacuum environment. Finally, the product was dried by a freeze-drying process and determined by ICP-AES (ICPS−8100, Shimadzu, Japan). The details of the in-situ surface modification process of the AlSi10Mg powder are displayed in Fig. 1, and the chemical compositions of different AlSi10Mg composite powders are listed in Table 1.

2.2 SLM process and material characterization

A self-developed SLM system (GDINM−D150, λ=1080 nm) with a maximum power of 500 W ytterbium fiber laser was used for the sample fabrication. Cubic samples for the microstructure characterization (10 mm × 10 mm × 10 mm),

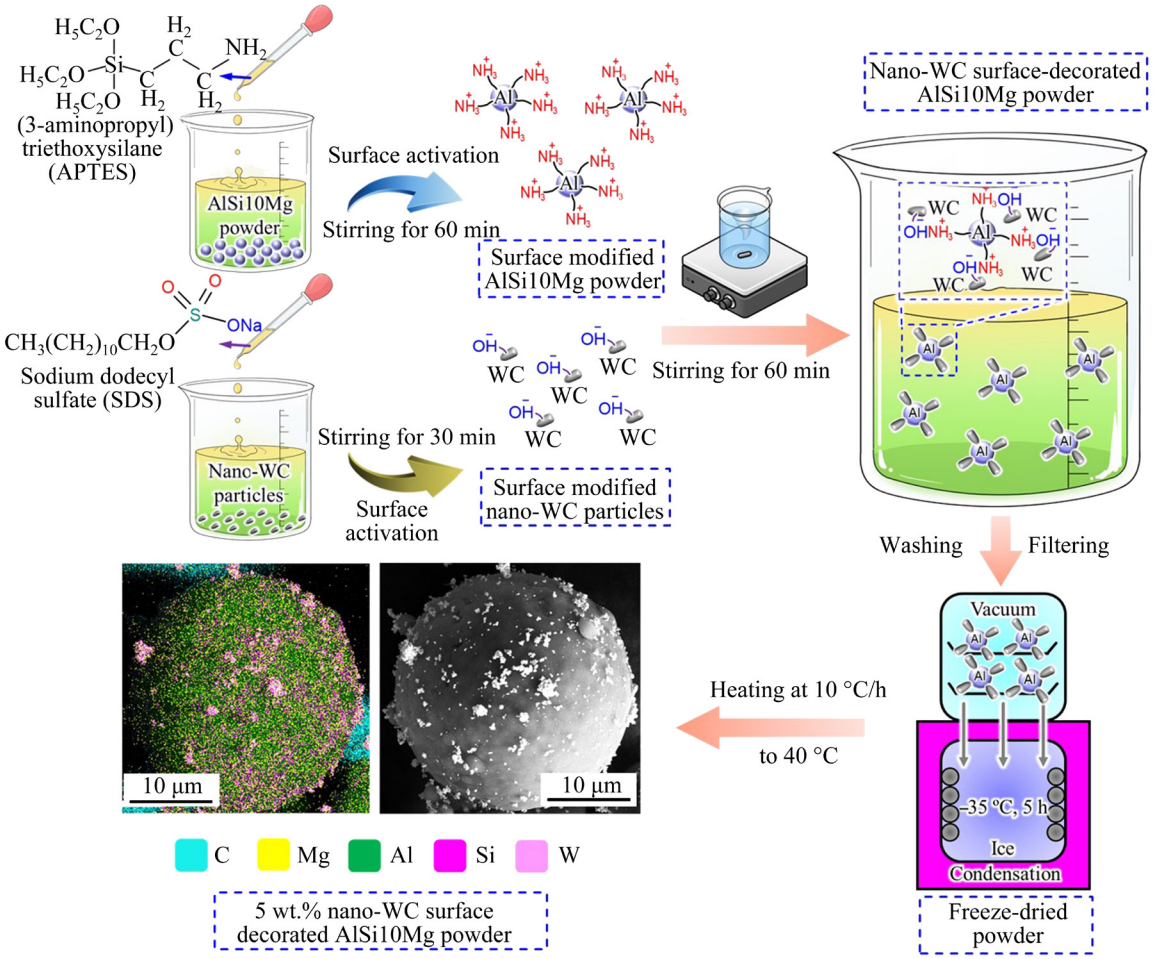

Fig. 1 Schematic of in-situ surface modification of AlSi10Mg powder

Table 1 Compositions of nano-WC surface modified AlSi10Mg powder (wt.%)

Powder	Si	Mg	Cu	Mn	Ti	WC	Al
1 wt.% WC/AlSi10Mg	9.74	0.23	0.01	0.01	0.01	0.92	Bal.
3 wt.% WC/AlSi10Mg	9.44	0.23	0.01	0.009	0.011	3.05	Bal.
5 wt.% WC/AlSi10Mg	9.45	0.21	0.01	0.01	0.012	5.10	Bal.

cylindric samples for wear performance (d10 mm × 5 mm), and tensile specimens for mechanical property test (73 mm × 11 mm × 3.5 mm) were processed by SLM under the protection of high-purity argon (99.999 vol.%). Optimized laser parameters were conducted with a laser power of 150 W, a scanning speed of 700 mm/s, a layer thickness of 30 μm, a hatch distance of 80 μm and a laser spot diameter of 50 μm. The forming strategy is zigzag in a single layer, and the rotation angle of the scanning strategy is 67° between every two neighboring layers.

The bulk samples were cut into two pieces and carefully polished by using a standard metallographic method, and then etched by Keller's reagent. Both cross-sectional and longitudinal sections of the microstructure were characterized by field emission scanning electron microscopy (SEM, Zeiss SIGMA−500) equipped with an energy dispersive spectrometer (EDS, BRUKER). Based on SEM micrographs, the average grain size was calculated by Image J software. Nanoparticles and element distribution were identified using an FEI Talos F200X transmission electron microscope (TEM). The samples for TEM observation were obtained by firstly mechanically thinned down to 20−50 μm, and then thinned again by using focused ion beam (FIB, FEI−SCIOS) equipment. The phase composition was investigated by an X-ray diffractometer (XRD, Rigaku Smartlab 9 kW) with Cu K_α radiation, operated at 40 kV and 100 mA, and a step size of 0.02 (°)/min and scanning speed of 4 (°)/min was used in XRD measurements. Mismatch calculations were performed using a CASTEP module in the Materials Studio software.

To explore the mechanical properties and wear behavior of the SLM nano-WC reinforced composites, all samples were mechanically polished accessively using different abrasive paper ranges from #80 to #2000 and then polished by a diamond grinding solution. All the mechanical and wear properties tests were conducted at room temperature. A VH1202 Vickers microhardness tester was used to measure the microhardness of these samples. All specimens were tested under 0.49 N load with a dwell time of 20 s. Static uniaxial tensile tests were performed according to the ASTM E8M standard with a crosshead rate of 1 mm/min. Average values were recorded after three measurements. The tribological properties of nano-WC/AlSi10Mg composites were performed using CETR UMT tester. GCr15 steel ball with a diameter of 6 mm was selected as the counterforce material. The wear test was applied under the following conditions: test load of 2 N, rotation radius of 1.5 mm, at a speed of 360 r/min for 10 min. The COF values were automatically recorded through the instrument during the wear tests, and the wear rate was calculated via a function in accordance with our previous work [21,22].

3 Results and discussion

3.1 Morphologies of composite powder

Unlike the traditional SEM morphology of aluminum powder decorated by ball-milled ceramic, all the as-prepared mixture powders synthesized by electrostatic self-assembly method showed a smooth and perfect spherical morphology in Fig. 2, in which no change in the size and morphology was observed compared to the pure AlSi10Mg powder. Consequently, these nano-WC particles decorated powder also had a similar good flowability to the AlSi10Mg powder. As shown in Fig. 2, the white nano-WC particles were homogeneously dispersed on the surface of the gray aluminum powder. As the addition content of WC increased from 1 wt.% to 5 wt.%, a few nano-WC aggregations disappeared on the aluminum powder surface. To further confirm the uniform distribution of nano-WC particles, the EDS mapping of 5 wt.%WC/AlSi10Mg sample was performed, as shown Fig. 3(g). The elements of tungsten (W) and carbon (C) were detected on the aluminum powder, which proved that the nano-sized particle was WC. The powder morphology features and EDS spectrum results demonstrated that this novel electrostatic self-assembly method had many advantages compared to the traditional process. For example, it can overcome the aggregation of WC nanoparticles by the electrostatic force, and it can maintain the sphericity of the matrix powders without any deformed shape.

3.2 Microstructure of SLM nano-WC/AlSi10Mg composites

Figure 3 demonstrated the heterogeneous microstructure of the regions adjacent to the track boundary due to the multiple lase melting and supercooling solidification processes, which was

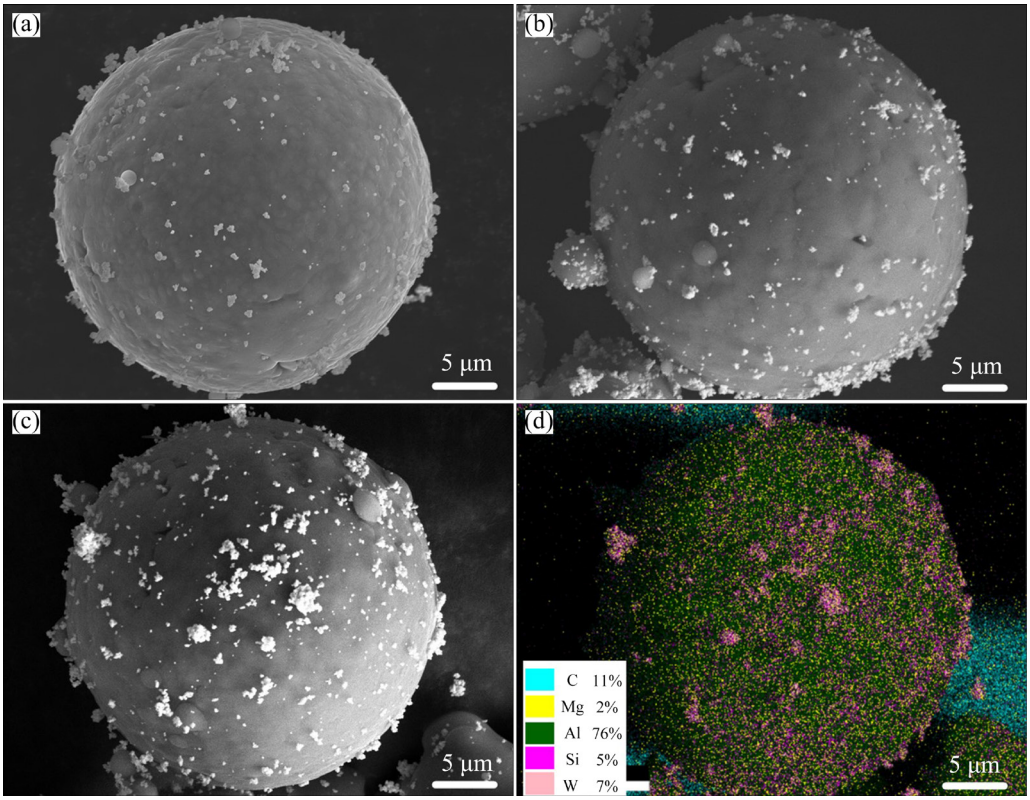

Fig. 2 Morphologies of as-prepared samples: (a) 1 wt.% nano-WC/AlSi10Mg powder; (b) 3 wt.% nano-WC/AlSi10Mg powder; (c) 5 wt.% nano-WC/AlSi10Mg powder; (d) EDS mapping of (c)

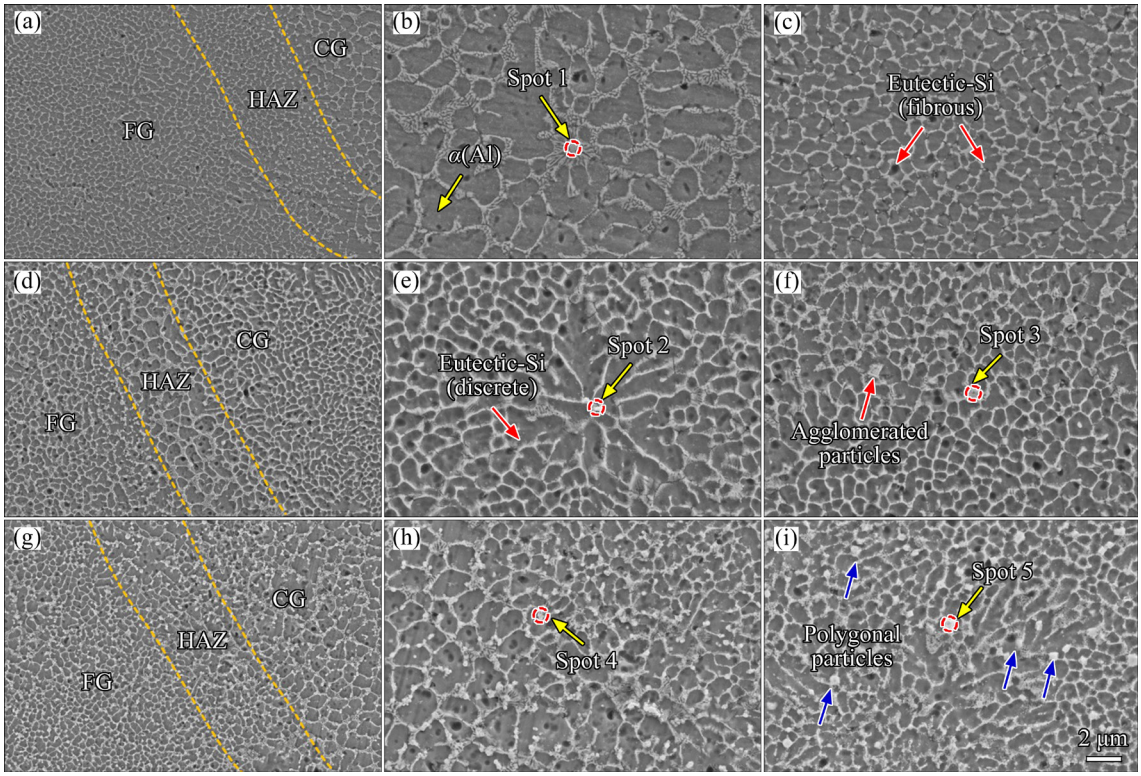

Fig. 3 SEM images and corresponding EDS points of nano-WC/AlSi10Mg composite in build direction reinforced with different contents of nano-WC: (a−c) 1 wt.%; (d−f) 3wt.%; (g−i) 5 wt.% (FG−Fine grain region; CG−Coarse grain region; HAZ−Heat-affected zone)

composed of fine grain region (FG), coarse grain region (CG), and heat-affected zone (HAZ). Meanwhile, the microstructure varied with nano-WC addition content. For the 1 wt.% decorated composites, the sample had a similar microstructure with the original SLM AlSi10Mg alloy, which consisted of the cellular α(Al) matrix (dark phase) and fibrous Si networks (gray phase). However, Fig. 3(b) also displayed a distinctive feature compared to AlSi10Mg alloy, and there were some round particles dispersed in the crystal boundaries. As the addition content of nano-WC particles was increased to 3 wt.%, the sample revealed some different features, as shown in Figs. 3(e, f). Firstly, the discrete eutectic Si particles were observed around the agglomerated particles (white phase). Secondly, some agglomerated particles appeared in the intercrystalline region (red arrows in Fig. 3(f)). The average grain size of 3 wt.% nano-WC/AlSi10Mg sample deceased from 0.80 to 0.41 μm compared to 1 wt.% nano-WC/AlSi10Mg sample. Numerous polygonal particles could be detected in the microstructure of the SLM 5 wt.% nano-WC reinforced composites (blue arrows in Fig. 3(i)). At the same time, a more refined grain size could also be obtained both in the fine crystalline and coarse crystalline regions of the 5 wt.% nano-WC/AlSi10Mg sample.

EDS analysis tests were conducted in different areas to further investigate the compositions of distributed particles in the SLM nano-WC/AlSi10Mg composites, as shown in Fig. 3. The detailed chemical composition results of those different particles are listed in Table 2. As identified from quantitative EDS results, three types of tungsten aluminide might be confirmed. $Al_{12}W$ phase was identified by the stoichiometry of the polygonal particle as marked at Spot 5 in Fig. 3(i). Al_4W in the form of acicular plates was located in the intracrystalline region, as labeled at Spot 3 in Fig. 3(f). Another possible tungsten aluminide was Al_5W, which could be informed from the stoichiometry of the round shape particle as marked at Spot 1 in Fig. 3(b) and Spot 4 in Fig. 3(h). The above tungsten aluminide might be formed by the in-situ reaction of WC and Al matrix during SLM process, which was also detected in the WC/Al composites [23].

Table 2 Chemical compositions of particles at location labeled in Fig. 3 (at.%)

Spot No.	Al	W	C	O
1	40.88	7.99	51.13	−
2	23.64	2.01	61.96	12.39
3	35.96	9.68	41.62	12.74
4	16.39	2.77	69.90	10.95
5	28.63	2.18	66.81	2.38

3.3 Microstructural evolution

XRD analysis and TEM observation were also conducted to explore the effects of nano-WC particles on the phase constituents and microstructural evolution in the SLM-fabricated AlSi10Mg samples. The main phases of the SLM nano-WC/AlSi10Mg samples with different WC contents were determined to be α(Al), Si, Mg_2Si, $Al_{12}W$, Al_5W and Al_4W, as detected in Fig. 4. By combining the SLM rapid melting/solidification process and Al−W phase diagram (Fig. 5(a)), the following sequence of the in-situ metallurgical reactions might account for the presence of the Al−W intermetallics in the SLM samples [21,22]:

On melting:

$$19Al(l)+3WC(s) \xrightarrow{1103\ K} 3Al_5W(s)+Al_4C_3(s) \quad (1)$$

On cooling:

$$Al(l)+(W) \xrightarrow{1925.6\ K} Al_2W(s) \xrightarrow{1621.9\ K} Al_4W(s) \quad (2)$$

On cooling:

$$Al(l)+Al_4W(s) \xrightarrow{1143.7\ K} Al_5W(s) \quad (3)$$

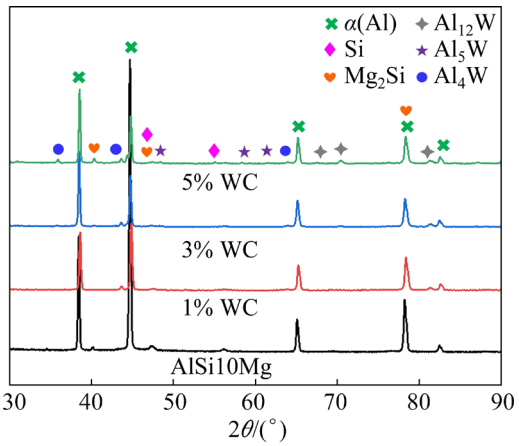

Fig. 4 XRD patterns of SLM samples with different nano-WC contents

As depicted in Fig. 5(b), different types of Al−W intermetallics (i.e., Al_4W and Al_5W) could stably exist within the SLM samples owing to the

quite low Gibbs free energy. Since SLM has ultra-high melting/cooling rates (10^6−10^8 K/s [2]), these metallurgical reactions can only arise from the decomposed nano-WC particles. Therefore, a few distinct peaks of Al−W phase were observed in the XRD pattern of SLM 5 wt.% nano-WC/AlSi10Mg sample. Interestingly, as presented in Reaction (1), although decomposed WC particles would react with Al melt to form the Al_4C_3 phase, it was hardly observed in the XRD pattern, which indicated that the content of in-situ formed Al_4C_3 phase was too low (<<5 wt.%) to be detected via the XRD.

Figure 6 shows the bright field images (BFIs) and main elements distribution of the SLM nano-WC/AlSi10Mg specimens with different WC additions. The α(Al) eutectic structures and the intergranular structures were composed of Si and Mg_2Si phases, which could be generated within the SLM nano-WC/AlSi10Mg samples based on the XRD results (Fig. 4) and the energy-dispersive X-ray spectroscopy (EDS) analysis (Fig. 6). Notably, as shown in Fig. 6(a), the microstructure of the SLM sample was dominated by coarse columnar grains (purple arrows) at the low content of WC (i.e., 1 wt.%). The nano-WC was mainly distributed among the dendrites as granular nano-particles (blue arrows). Differently, as the WC content increased to 5 wt.%, as depicted in Fig. 6(b), the microstructure of the SLM sample consisted of equiaxed grains (pink arrows) with an average size about 0.83 μm (purple arrows). Moreover, polygonal W-rich nanoparticles not only existed in

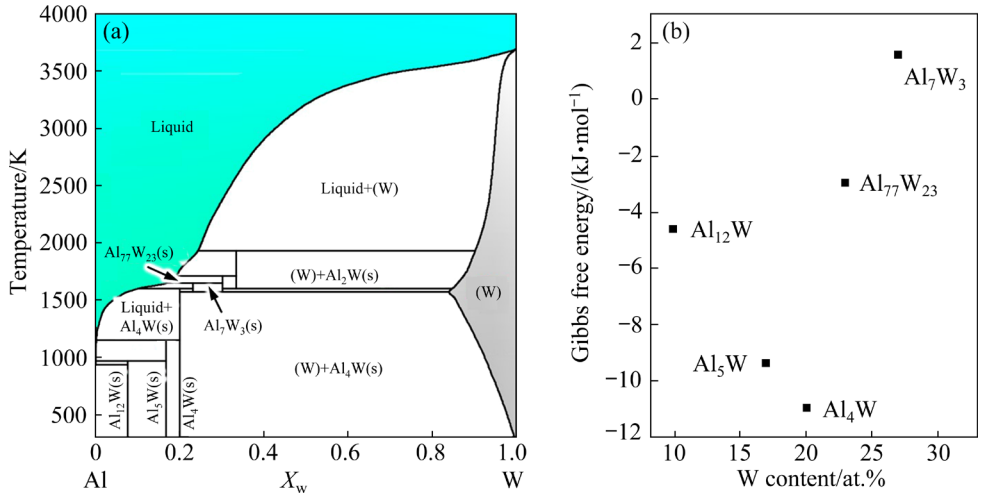

Fig. 5 Al−W phase diagram [24] (a) and Gibbs free energy for Al−W intermetallics [25] (b)

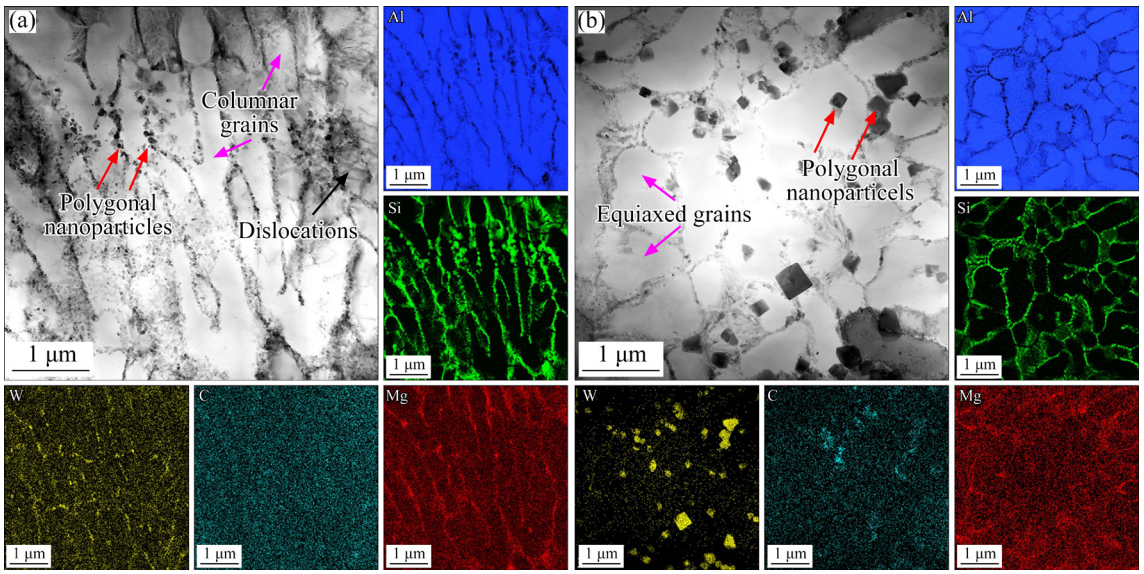

Fig. 6 Bright field image and main elements distribution: (a) SLM 1 wt.% nano-WC/AlSi10Mg sample; (b) SLM 5 wt.% nano-WC/AlSi10Mg sample

the intergranular structures, but also appeared with equiaxed grains (red arrows). It might be ascribed to the massively introduced nano-WC particles and in-situ formed Al−W intermetallics, leading to the transition of columnar grains to fine equiaxed grains in the SLM nano-WC/AlSi10Mg samples.

In order to further explore the types and distribution of the in-situ generated nanoparticles in the SLM nano-WC/AlSi10Mg samples, more TEM observation results of these nanoparticles taken from Fig. 6 are presented in Fig. 7. As detected in Fig. 7(a), the selected nanoparticles were proven as the Al_5W phase according to the selected area electron diffraction (SAED) pattern. Moreover, the crystallographic relationship between α(Al) and Al_5W could be determined as $[110]_{\alpha(Al)}//[\bar{1}2\bar{1}3]_{Al_5W}$ and $(002)_{\alpha(Al)}//(104)_{Al_5W}$, indicating a good coherent interface between these two phases. Moreover, the element of C was enriched at the Point I (Fig. 7(a)), indicating that the Al_5W phase was formed and grew around the decomposed nano-WC particles. Notably, the diffraction rings (i.e., $(012)_{Al_5W}$ and $(022)_{Al_5W}$) in the SAED image also proved the formation and enrichment of a large number of fine nano-Al_5W particles. To further confirm the lattice mismatch, the interface condition between the α(Al) primitive cell (cubic, $Fm\bar{3}m$) and the Al_5W primitive cell (hexagonal, $P63$) was examined, as shown in Fig. 8. It can be calculated according to Eq. (4):

$$\delta=\frac{|\alpha_{Al(h_1k_1l_1)}-\alpha_{Al_5W(h_2k_2l_2)}|}{\alpha_{Al(h_1k_1l_1)}}\times100\% \quad (4)$$

where δ is the lattice mismatch, α is the lattice parameters of the α(Al) phase and the Al_5W phase in the supercell, respectively. Hence, the lattice mismatch of the interface between $(002)_{\alpha(Al)}$ and $(104)_{Al_5W}$ was calculated as 4.7% (<5%), illustrating a stable coherent interface between α(Al) phase and Al_5W phase, as observed in the high-resolution TEM (HRTEM I) (Fig. 7(a)).

As presented in Fig. 7(c), polygonal nano-Al_4W particles were determined via SAED pattern and the corresponding EDS results. Different from the Al_5W/α(Al) interface, an incoherent interface

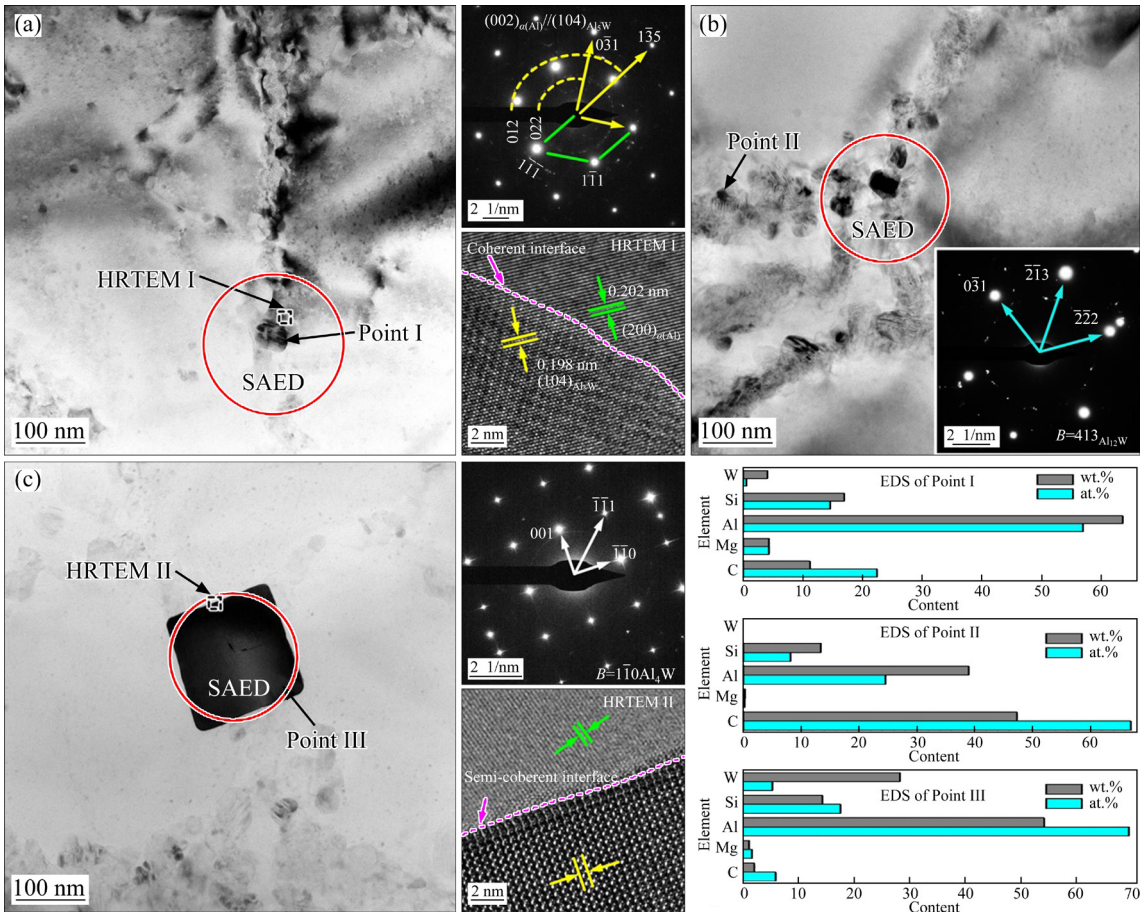

Fig. 7 Nanoparticles detected in SLM nano-WC/AlSi10Mg samples: (a) Al_5W phase; (b) $Al_{12}W$ phase; (c) Al_4W phase

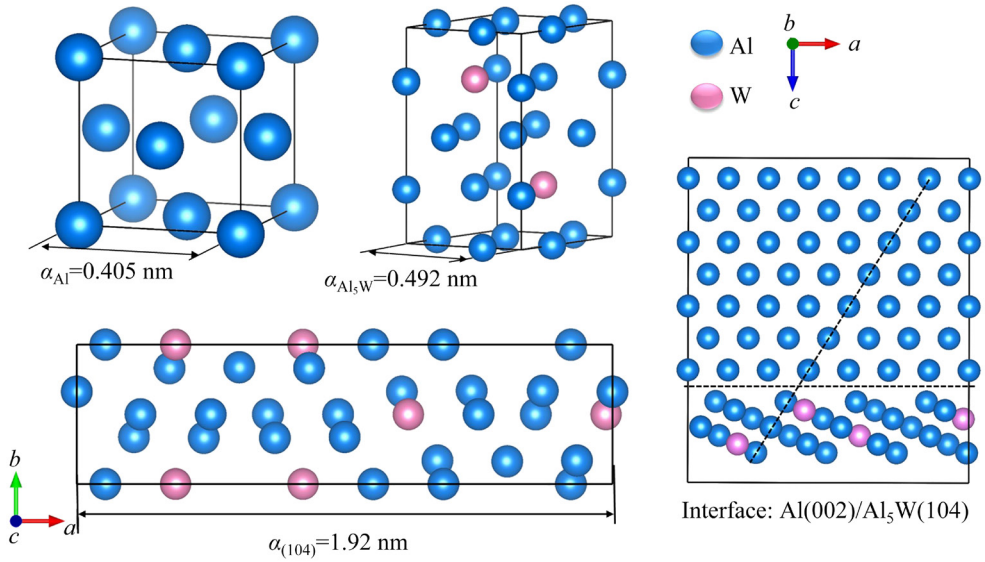

Fig. 8 Calculation of $(002)_{\alpha(Al)}/(104)_{Al_5W}$ interface

between the $(110)_{Al_4W}$ and $(111)_{\alpha(Al)}$ was witnessed via the HRTEM result. The incoherent interface played a vital role in dislocation pinning (black arrows in Fig. 6(a)). Interestingly, $Al_{12}W$ phase, an Al-W metallic compound that was not detected in the XRD pattern, was identified by SAED, as displayed in Fig. 7(b). Its formation follows the process shown below [24]:

On cooling:

$$Al(l)+Al_5W(s)\xrightarrow{970.2\ K}Al_{12}W(s)\xrightarrow{933.5\ K}(Al) \quad (5)$$

Since $Al_{12}W$ phase was formed from the decomposed nano-Al_5W particles and might be further decomposed during the solidification, only a very small amount of granular nano-$Al_{12}W$ compounds could exist within the SLM samples. Besides, as revealed in Fig. 7(b), the EDS results of Point II exhibited extremely high C and Al element contents, while the W element content is zero. Combined with Reaction (1), it might be a few nano-Al_4C_3 particles generated during the melting of WC. However, its content was too low to be detected from the XRD pattern.

In conclusion, owing to the high temperature of the laser molten pool, the introduced nano-WC particle is partially dissolved into the α(Al) matrix and reacts with the main elements to form a series of Al−W intermetallics. As the SLMed melt pool begins to solidify, the high melting nano-WC and Al−W compound particles prefer to form. Since the lattice mismatch between $(104)_{Al_5W}$ phase and $(002)_{\alpha(Al)}$ phase is 4.7%, according to Turnbull and Vonnegut's report, the critical nucleation undercooling (ΔT_n) shows a positive correlation with the change of the lattice misfit (δ), which follows Eq. (6) [26]:

$$\Delta T_n=\frac{C_E}{\Delta S_V} \quad (6)$$

where C_E is the coefficients of elasticity and ΔS_V is the entropy of phase transition per volume.

Hence, the Al_5W phase has a coherent relationship with α(Al), and promotes the columnar-to-equiaxed transition, further inhibiting the growth of grains. Also, it can serve as an effective heterogeneous nucleants to promote the precipitation of Mg_2Si. This phenomenon is similar to the traditional grain refiners, as reported by WANG et al [27], where TiB_2 can not only refine the grain size of SLM-fabricated TiB_2/AlMgScZr composite grains, but also significantly promote the precipitation of second-phase particles, such as Al_3Sc and Al_3Zr.

3.4 Mechanical properties

Figures 9 and 10 show the mechanical properties and fracture morphologies of the SLM nano-WC/AlSi10Mg samples, respectively. As displayed in Fig. 9, compared with the SLM AlSi10Mg sample, the in-situ introduction of nano-WC particles had a significant improvement in its strength and microhardness (HV). The average microhardness increased from (113.1±5.28) ($HV_{0.05}$) of the AlSi10Mg sample to (141.7±8.32) ($HV_{0.05}$) of

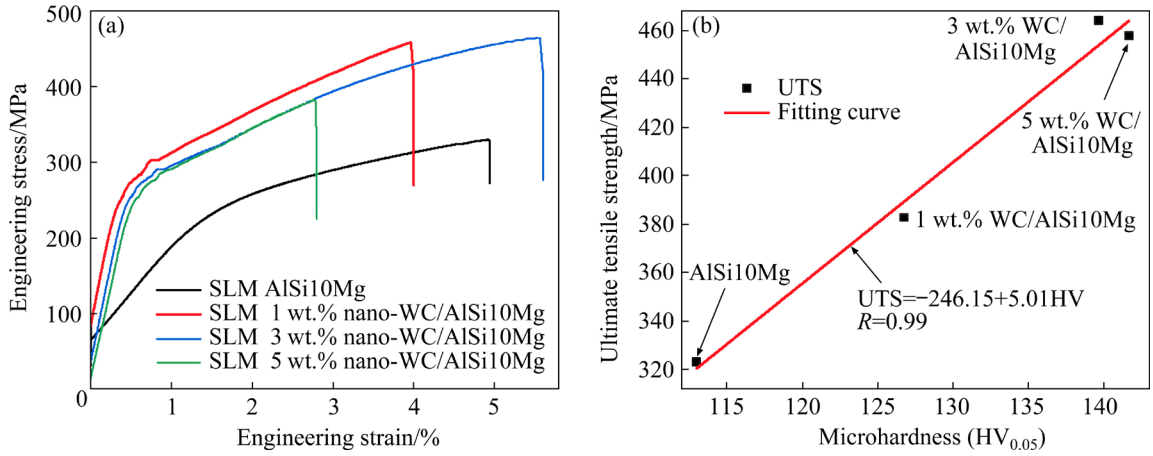

Fig. 9 Mechanical properties of SLM nano-WC/AlSi10Mg samples with different WC contents: (a) Engineering stress−strain curves; (b) UTS−microhardness relationship

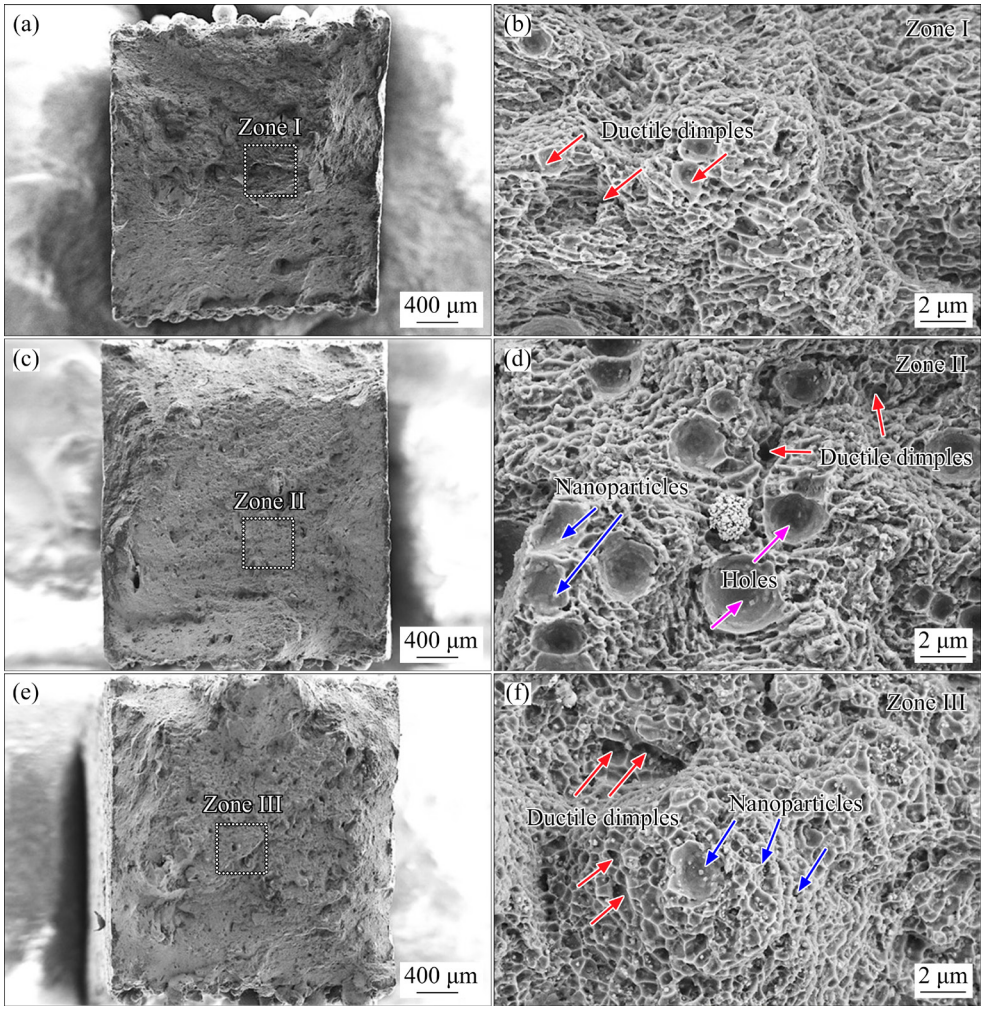

Fig. 10 Fracture morphologies of samples: (a, b) SLM 1 wt.% nano-WC/AlSi10Mg; (c, d) SLM 3 wt.% nano-WC/AlSi10Mg; (e, f) SLM 5 wt.% nano-WC/AlSi10Mg

the SLM 5wt.%WC/AlSi10Mg. This hardness enhancement was mainly accomplished by the high content of in-situ synthesis of tungsten aluminide nanoparticles in the Al matrix. NIU et al [28] found that the formation of $Al_{12}W$ particles could be attributed to the high strength by the extra-electron

induced covalent strengthening mechanism. WANG et al [29] also confirmed the Al_4W, Al_5W and $Al_{12}W$ particles improve the hardness of Al matrix composite based on first-principles calculation, and Al_4W has the highest microhardness (14.26 GPa) among those tungsten aluminide particles.

The ultimate tensile strength (UTS) and elongation increased from (323.3±10.25) MPa and (4.9±1.21)% of the AlSi10Mg sample to (464.1±8.68) MPa and (5.6±0.95)% of the SLM 3 wt.% WC/AlSi10Mg sample, respectively. With the increase of WC content, the relationship between UTS and hardness in SLM nano-WC/AlSi10Mg samples is: UTS=−246.15+5.01HV (R^2=0.99), presenting excellent linear correlation. Although the introduction of nano-WC particles greatly contributes to the strength of the AlSi10Mg alloy, the UTS shows a decreasing trend (arrows in Fig. 9(b)) once the WC addition is high (e.g., 5 wt.%).

At the low content of WC addition, the microstructure was dominated by the coarse columnar grains (Fig. 6(a)). Thus, as shown in Fig. 10(a), the fracture surface was composed of a large number of small dimples (red arrows). When the WC contents were gradually raised, the coherent nano-Al_5W phase would greatly promote the formation of the equiaxed grains (Figs. 6(a, b)), further leading to a substantial increase in its UTS and elongation. Therefore, the fracture surface was prevailed by several ductile dimples (Fig. 10(b)). With the WC addition further increasing, a great number of intermetallics (blue arrows) like incoherent nano-Al_4W particles (Fig. 7(c)) would boost its brittleness. Particularly, the in-situ formed Al_4C_3 particles would weaken the bonding strength of the WC and the aluminum matrix, thereby leading to a decrease in its strength and elongation (Fig. 9). Therefore, fracture morphology of the SLM 5 wt.% WC/AlSi10Mg sample consisted of huge quantities of tiny ductile dimples and brittle nanoparticles (Fig. 10(c)).

The typical COF curves of nano-WC reinforced AlSi10Mg with different WC contents are presented in Fig. 11. Obviously, all the specimens exhibited the same COF characteristic. The 3 wt.% nano-WC/AlSi10Mg sample had the lowest average COF values and demonstrated stable COF evolutions during the whole test procedure. Meanwhile, the wear rate of 3 wt.% nano-WC/

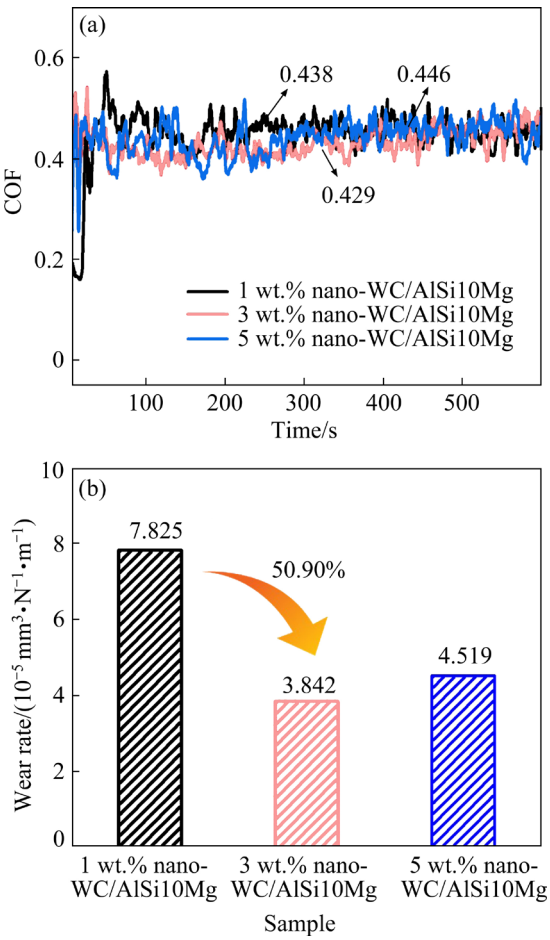

Fig. 11 Coefficient of friction curves (a) and wear rate (b) of different contents nano-WC reinforced AlSi10Mg samples

AlSi10Mg also was the lowest and the wear rate of this sample was 50.90% lower than that of 1 wt.% nano-WC/AlSi10Mg sample. Figure 12 shows the wear rate and wear morphologies of the different contents nano-WC reinforced AlSi10Mg samples. The wear tracks on the surface of all testing parts presented ploughing grooves, delamination cracks and wear debris, which meant that the wear mechanism of the nano-WC reinforced Al composites was mainly adhesive wear. The surface damage of the 1 wt.% nano-WC/AlSi10Mg sample was serious, with deep wear grooves and severe plastic deformation along the sliding direction. Evidently, the smallest amount of debris and delamination cracks were observed in the 3 wt.% nano-WC/AlSi10Mg sample. On the contrary, the wear surface of the 5 wt.% nano-WC/AlSi10Mg sample contained more wear debris and delamination cracks, which might be generated by the high strain levels of their brittleness particles

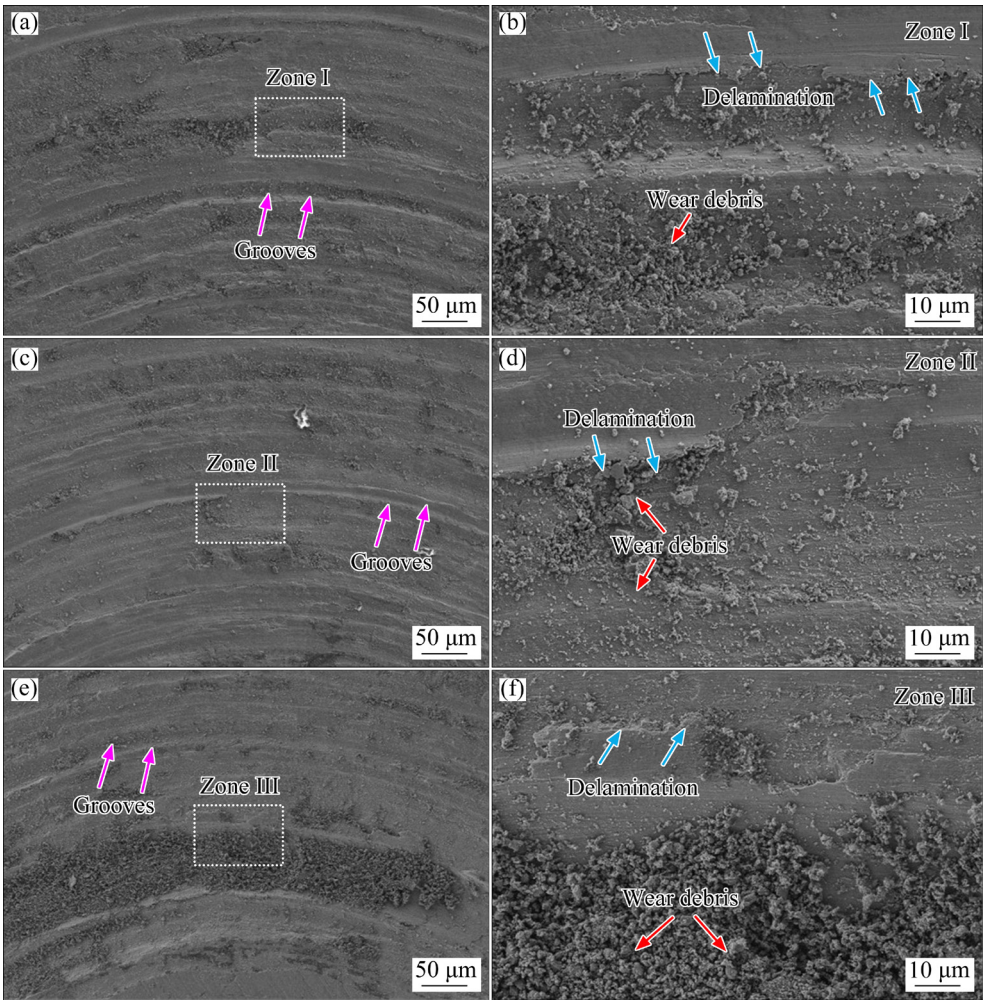

Fig. 12 Wear morphologies of nano-WC reinforced AlSi10Mg samples: (a, b) 1 wt.% nano-WC/AlSi10Mg; (c, d) 3 wt.% nano-WC/AlSi10Mg; (e, f) 5 wt.% nano-WC/AlSi10Mg

distributed in the Al matrix, such as Al_4W, $Al_{12}W$ and Al_4C_3 phases. This trend of wear morphologies was consistent with the change of wear rate, as shown in Fig. 11(b). Figures 12(e, f) revealed that the debris of the 5 wt.% nano-WC/AlSi10Mg sample was larger than that of the other samples, and the size was 2−5 μm, which indicated that the wear mechanism changed from adhesive wear to slightly abrasive wear.

The mechanical strengthening and wear properties enhancement of the SLMed nano-WC reinforced AlSi10Mg composites are ascribed to the fine-grain strengthening and second-phase strengthening. The fine-grain strengthening is estimated by the following equation:

$$\Delta\sigma_{\text{Hall-Petch}}=kd^{-1/2} \tag{7}$$

where k denotes a constant and d is the grain size. For aluminum alloy, the constant of k is set as 50 MPa·μm$^{1/2}$ [30]. According to Fig. 3(d), the average grain size of 3 wt.% WC/AlSi10Mg is measured as 0.41 μm. Therefore, the fine-grain strengthening contribution is estimated to be ~78.09 MPa.

In the second-phase strengthening, according to the Orowan strengthening mechanism, the dispersion strengthening contribution of nano-WC particles and the Al-W intermetallics is calculated following Eq. (8) [31]:

$$\Delta\sigma_{\text{Orowan}}=\frac{\varphi G_{\text{m}} b}{d_{\text{p}}}\left(\frac{6V_{\text{p}}}{\pi}\right)^{1/3} \tag{8}$$

where the constants of G_{m}, b, and φ are selected according to our previous study [12]. For the SLM-fabricated 3 wt.% WC/AlSi10Mg alloy, the d_{p} represents the particle size of nano-WC (200 nm), and V_{p} denotes the volume fraction of WC addition (~0.53%). Here, the whole volume fraction of the nano-WC and the in-situ formed Al−W inter-

metallics are simplified approximately equal to the volume fraction of the original WC. As calculated by Eq. (8), the dispersion strengthening contribution is estimated at ~76.1 MPa. Finally, the calculated whole strengthening contribution of the 3 wt.% nano-WC addition is around 154.19 MPa, which is slightly high than that of test values.

4 Conclusions

(1) AlSi10Mg powders were in-situ surface modified with different nano-WC contents using an electrostatic assembly method. The nano-WC/AlSi10Mg alloy with fine equiaxed grains composed of the in-situ formed Al−W reinforcements (i.e., Al_5W, Al_4W and $Al_{12}W$) was fabricated using SLM.

(2) Al_5W/α(Al) interface presented a superb coherent interface ($[110]_{\alpha(Al)}//[\bar{1}\bar{2}13]_{Al_5W}$ and $(002)_{\alpha(Al)}//(104)_{Al_5W}$) with a low lattice mismatch (4.7%). Under the synergistic effect of the coherent nano-Al_5W phase and other multiple Al−W inter-metallics, UTS and elongation increased from (323.3±10.25) MPa and (4.9±1.21)% of the AlSi10Mg sample to (464.1±8.68) MPa and (5.6±0.95)% of the SLM 3 wt.%WC/AlSi10Mg sample, respectively. Meanwhile, SLM 3 wt.% WC/AlSi10Mg composite attained the lowest average coefficient of friction (0.429) and wear rate (3.842×10^{-5} mm^3/(N·m)).

(3) In summary, a series of tungsten aluminide particles reinforced AlSi10Mg composites were successfully in-situ fabricated using the SLM method. The major findings of this research work prove that the nano-WC particle also has the same grain refinement and strengthening effects as the traditional effective nucleants for α(Al).

CRediT authorship contribution statement

Jiang-long YI: Conceptualization, Methodology, Writing − Original draft; **Han-lin LIAO:** Investigation, Resources; **Cheng CHANG:** Data curation, Writing − Review & editing; **Xing-chen YAN:** Data curation, Formal analysis; **Min LIU:** Investigation, Resources, Project administration; **Ke-song ZHOU:** Resources, Project administration.

Declaration of competing interest

The authors declare that they have no known competing financial interests or personal relationships that could have appeared to influence the work reported in this paper.

Acknowledgments

This work was supported by the Technical Project of Guangdong Province, China (Nos. 2020B090923002, 2021A1515011756), GDAS' Project of Science and Technology Development, China (No. 2021GDASYL-20210302006), Sciences Platform Environment and Capacity Building Projects of GDAS, China (No. 2021GDASYL-20210102005), Key R&D Program of Guangdong Province, China (No. 2020B090923002), Guangdong Special Support Program, China (No. 2019BT02C629), and Guangdong Basic and Applied Basic Research Fund, China (Nos. 2020A1515111031, 2021A1515010939).

References

[1] CHANG Cheng, YAN Xing-chen, BOLOT R, GARDAN J, GAO Shuo-hong, LIU Min, LIAO Han-lin, CHEMKHI M, DENG Si-hao. Influence of post-heat treatments on the mechanical properties of CX stainless steel fabricated by selective laser melting [J]. Journal of Materials Science, 2020, 55: 8303−8316.

[2] CHANG Cheng, YUE Shu-jun, LI Wei-rong, LU Li, YAN Xing-chen. Study on microstructure and tribological behavior of the selective laser melted MgZnCa alloy [J]. Materials Letters, 2022, 309: 131439.

[3] DONG Dong-dong, CHANG Cheng, WANG Hao, YAN Xing-chen, MA Wen-you, LIU Min, DENG Si-hao, GARDAN J, BOLOT R, LIAO Han-lin. Selective laser melting (SLM) of CX stainless steel: Theoretical calculation, process optimization and strengthening mechanism [J]. Journal of Materials Science & Technology, 2020, 73: 151−164.

[4] CHRISTOPH L, MANFRED P. Titanium and titanium alloys: Fundamentals and applications [M]. Weinheim, Wiley-VCH, 2003.

[5] WANG Pei, ECKERT J, PRASHANTH K G, WU Ming-wei, KABAN I, XI Li-xia, SCUDINO S. A review of particulate-reinforced aluminum matrix composites fabricated by selective laser melting [J]. Transactions of Nonferrous Metals Society of China, 2020, 30: 2001−2034.

[6] AKBARI M, KHALKHALI A, KESHAVARZ S M E, SARIKHANI E. Investigation of the effect of friction stir processing parameters on temperature and forces of Al−Si aluminum alloys [J]. Proceedings of The Institution of Mechanical Engineers Part L−Journal of Materials−Design and Applications, 2017, 232: 323−327.

[7] WANG Min, SONG Bo, WEI Qing-song, SHI Yu-sheng. Improved mechanical properties of $AlSi_7Mg$/nano-SiC_p composites fabricated by selective laser melting [J]. Journal of Alloys and Compounds, 2019, 810: 151926.

[8] XI Li-xia, DING Kai, ZHANG Han, GU Dong-dong. In-situ

synthesis of aluminum matrix nanocomposites by selective laser melting of carbon nanotubes modified Al−Mg−Sc−Zr alloys [J]. Journal of Alloys and Compounds, 2022, 891: 162047.

[9] LI Yu-xin, GU Dong-dong, ZHANG Han, XI Li-xia. Effect of trace addition of ceramic on microstructure development and mechanical properties of selective laser melted AlSi10Mg alloy [J]. Chinese Journal of Mechanical Engineering, 2020, 33: 33.

[10] GU Dong-dong, HAGEDORN Y C, MEINERS W, MENG Guang-bin, BATISTA R J S, WISSENBACH K, POPRAWE R. Densification behavior, microstructure evolution, and wear performance of selective laser melting processed commercially pure titanium [J]. Acta Materialia, 2012, 60: 3849−3860.

[11] SONG Bo, ZHAO Xiao, LI Shuai, HAN Chang-jun, WEI Qing-song, WEN Shi-feng, LIU Jie, SHI Yu-sheng. Differences in microstructure and properties between selective laser melting and traditional manufacturing for fabrication of metal parts: A review [J]. Frontiers of Mechanical Engineering, 2015, 10: 111−125.

[12] FAN Zhen-hua, YAN Xing-chen, FU Zhi-yong, NIU Ben, CHEN Jun-fu, HU Yong-jun, CHANG Cheng, YI Jiang-long. In situ formation of D022-Al_3Ti during selective laser melting of nano-TiC/AlSi10Mg alloy prepared by electrostatic self-assembly [J]. Vacuum, 2021, 188: 110179.

[13] TAN Hua, HAO Da-peng, AL-HAMDANI K, ZHANG Feng-ying, XU Zheng-kai, CLARE A T. Direct metal deposition of TiB_2/AlSi10Mg composites using satellited powders [J]. Materials Letters, 2018, 214: 123−126.

[14] GAO Chao-feng, XIAO Zhi-yu, LIU Zhong-qiang, ZHU Quan-li, ZHANG Wei-wen. Selective laser melting of nano-TiN modified AlSi10Mg composite powder with low laser reflectivity [J]. Materials Letters, 2019, 236: 362−365.

[15] LI Rui-di, WANG Min-bo, LI Zhi-ming, CAO Peng, YUAN Tie-chui, ZHU Hong-bin. Developing a high-strength Al−Mg−Si−Sc−Zr alloy for selective laser melting: Crack-inhibiting and multiple strengthening mechanisms [J]. Acta Materialia, 2020, 193: 83−98.

[16] AKBARI M, ASADI P, ZOLGHADR P, KHALKHALI A. Multicriteria optimization of mechanical properties of aluminum composites reinforced with different reinforcing particles type [J]. Proceedings of the Institution of Mechanical Engineers Part E−Journal of Process Mechanical Engineering, 2017, 232: 323−337.

[17] MARTIN J H, YAHATA B D, HUNDLEY J M, MAYER J A, SCHAEDLER T A, POLLOCK T M. 3D printing of high-strength aluminium alloys [J]. Nature, 2017, 549: 365−369.

[18] LI X P, JI G, CHEN Z, ADDAD A, WU Y, WANG H W, VLEUGELS J, HUMBEECK J V, KRUTH J P. Selective laser melting of nano-TiB_2 decorated AlSi10Mg alloy with high fracture strength and ductility [J]. Acta Materialia, 2017, 129: 183−193.

[19] LI Wei, XU Pei-quan, WANG Yue-yue, ZOU Yun, GONG Hong-ying, LU Feng-gui. Laser synthesis and microstructure of micro- and nano-structured WC reinforced Co-based cladding layers on titanium alloy [J]. Journal of Alloys and Compounds, 2018, 749: 10−22.

[20] SIEGEL D J, HECTOR L G, ADAMS J B. Adhesion, stability, and bonding at metal/metal-carbide interfaces: Al/WC [J]. Surface Science, 2012, 498: 321−336.

[21] YAN Xing-chen, CHANG Cheng, DENG Zhao-yang, LU Bing-wen, CHU Qing-kun, CHEN Xing-chi, MA Wen-you, LIAO Han-lin, LIU Min. Microstructure, interface characteristics and tribological properties of laser cladded NiCrBSi−WC coatings on PH 13-8 Mo steel [J]. Tribology International, 2021, 157: 106873.

[22] YAN Xing-chen, GAO Shu-hong, CHANG Cheng, HUANG Jian, KHANLARI K, DONG Dong-dong, MA Wen-you, FENINECHE N, LIAO Han-lin, LIU Min. Effect of building directions on the surface roughness, microstructure, and tribological properties of selective laser melted Inconel 625 [J]. Journal of Materials Processing Technology, 2021, 288: 116878.

[23] LEKATOU A, KARANTZALIS A E, EVANGELOU A, GOUSIA V, KAPTAY G, GACSI Z, BAUMLI P, SIMON A. Aluminium reinforced by WC and TiC nanoparticles (ex-situ) and aluminide particles (in-situ): Microstructure, wear and corrosion behaviour [J]. Materials & Design, 2015, 65: 1121−1135.

[24] WANG Pei-sheng, XIONG Wei, KATTNER U R, CAMPBELL C E, LASS E A, KONTSEVOI O Y, OLSON G B. Thermodynamic re-assessment of the Al−Co−W system [J]. Calphad, 2017, 59: 112−130.

[25] RAJAMURE R S, VORA H D, SRINIVASAN S G, DAHOTRE N B. Laser alloyed Al−W coatings on aluminum for enhanced corrosion resistance [J]. Applied Surface Science, 2015, 328: 205−214.

[26] TURNBULL D, VONNEGUT B. Nucleation catalysis [J]. Industrial Engineering Chemistry, 1952, 44: 1292−1298.

[27] WANG Ji-hao, LIU Tong-liu, LUO Liang-shun, CAI Xiao-ye, WANG Bin-bin, ZHAO Jun-hao, CHENG Zong-hui, WANG Liang, SU-Yanqing, XUE Xiang, GUO Jing-jie. Selective laser melting of high-strength TiB_2/AlMgScZr composites: microstructure, tensile deformation behavior, and mechanical properties [J]. Journal of Materials Research and Technology, 2022, 16: 786−800.

[28] NIU Hai-yang, CHEN Xing-qiu, LIU Pei-tao, XING Wei-wei, CHENG Xi-yue, LI Dian-zhong, LI Yi-yi. Extra-electron induced covalent strengthening and generalization of intrinsic ductile-to-brittle criterion [J]. Scientific Reports, 2012, 2: 1−6.

[29] WANG Chan, LIANG Shu-hua, CUI Jie, WANG Xian-hui, WEI Yan-ni. First-principles study of the mechanical and thermodynamic properties of Al_4W, Al_5W and $Al_{12}W$ under pressure [J]. Vacuum, 2019, 169: 108844.

[30] GUTIERREZ-URRUTIA I, MUÑOZ-MORRIS M A, MORRIS D G. Contribution of microstructural parameters to strengthening in an ultrafine-grained Al−7%Si alloy processed by severe deformation [J]. Acta Materialia, 2007, 55: 1319−1330.

[31] LIU G, ZHANG G J, JIANG F, DING X D, SUN Y J, SUN J, MA E. Nanostructured high-strength molybdenum alloys with unprecedented tensile ductility [J]. Nature Materials, 2013, 12: 344−350.

原位表面改性的纳米 WC/AlSi10Mg 合金增强机制

易江龙[1]，廖汉林[2,3]，常 成[2,3]，闫星辰[2]，刘 敏[2]，周克崧[1,2]

1. 广东工业大学 材料与能源学院，广州 510006；
2. 广东省科学院 新材料研究所，现代材料表面工程技术国家工程实验室，
广东省现代表面工程技术重点实验室，广州 510651；
3. ICB UMR 6303, CNRS, Univ. Bourgogne Franche-Comté, UTBM,90010, Belfort, France

摘 要：采用静电自组装工艺合成−系列不同纳米 WC 含量的表面改性 AlSi10Mg 粉末，并使用激光选区熔化(SLM)技术制备纳米 WC/AlSi10Mg 复合材料。结果表明，SLM 制备的纳米 WC/AlSi10Mg 材料中形成多种 Al−W 金属间化合物相，通过$(002)_{\alpha(Al)}//(104)_{Al_5W}$的取向关系，证实具有 4.7%的低晶格失配度的 Al/Al_5W 可形成良好共格界面。纳米 WC 颗粒和 Al−W 相可促使柱状晶转变为等轴晶，获得精细的等轴晶组织。同时，SLM 制备的 3%(质量分数)纳米 WC/AlSi10Mg 复合材料具有最优的力学性能，抗拉强度为(464.1±8.68) MPa，伸长率为(5.6±0.95)%。此外，与其他 WC/AlSi10Mg 复合材料相比，SLM 制备的 3%WC/AlSi10Mg 样品的平均摩擦因数和磨损率最低，分别为 0.429 和 3.842×10^{-5} $mm^3/(N\cdot m)$。力学和磨损性能的提升主要归因于晶粒细化和第二相析出强化作用。

关键词：原位改性；激光选区熔化；纳米 WC；AlSi10Mg；力学性能

(Edited by Bing YANG)